Acoustic tokamak with strongly coupled toroidal bubbles

A. Caumont, O. Stephan ⬤, E. Bossy ⬤, B. Dollet, C. Quilliet, and P. Marmottant ⬤[*]

Univ. Grenoble Alpes, CNRS, LIPhy, F-38000 Grenoble, France

Gas bubbles stabilized in toroidal 3D-printed cages are good acoustic resonators with an unusual topology. We arrange them in a circular array to obtain what we call an "acoustic tokamak" because of the torus shape of the whole array. We demonstrate experimentally and theoretically that the system features several acoustic modes resulting from the acoustic interaction between tori. The fundamental acoustic mode has a much lower frequency than that of the individual bubbles. The acoustic field along the circle inside the acoustic tokamak is remarkably homogeneous, as shown by our 3D simulations.

I. INTRODUCTION

Bubbles in a liquid are a configuration of choice to create acoustic metamaterials, since they display a strong acoustic resonance, while their size is much smaller than the wavelength. It has been shown that the coupling between subwavelength objects can result in very localized emission patterns; see, for instance, the study of soda cans in air in [1].

Recently we showed that we could obtain long-lasting bubbles of arbitrary shapes such as cubes [2], polyhedra [3], and tori in 3D-fabricated cages [4]. Among these shapes, the toroidal one is particularly useful to shape the acoustic field. Under excitation a toroidal bubble emits an acoustic field with a first particularity: there is a vanishing gradient of the acoustic field at the center of the torus. Contrary to usual oscillating sources it is then possible to obtain a uniform acoustic field, for instance, in a tunnel of aligned coaxial tori [4]. Note that toroidal resonators within metamaterials have been addressed in electromagnetics [5,6] showing unique properties such as the Hofstadter's butterfly spectrum [7] when the resonance frequency is periodically detuned.

Another particularity of the acoustics of toroidal bubbles lies in its interaction with other toroidal bubbles. Oscillating bubbles are coupled through the pressure they emit, which modifies their natural resonance frequency [8–13]. A couple of toroidal bubbles have stronger coupling, as compared to a couple of spherical bubbles. Indeed, if we consider a couple of spherical bubbles of radius R that have an individual resonance pulsation frequency ω_0 [4,14], their common resonance frequency drops to the value $\omega = \omega_0/\sqrt{1 + R/d}$ (fundamental mode) with d their center-to-center distance [15]. At contact $d = 2R$, the resonance drops to $\omega = \omega_0\sqrt{2/3} \simeq 0.82\omega_0$. If we consider a couple of coaxial toroidal bubbles of grand radius R and of small radius b their fundamental frequency obeys $\omega = \omega_0/\sqrt{1 + f_t(R/d)/\ln(8R/b)}$, with $f_t(\xi) = 2\xi K(4\xi^2/(4\xi^2 + 1))/\sqrt{4\xi^2 + 1}$ an interaction factor involving K the complete elliptic integral of the first kind [4]. At contact $d = 2b$, the resonance drops to $\omega \simeq 0.74\omega_0$ assuming $R/b = 7.4$, a value that weakly depends on R/b.

The classical arrangement of coupled oscillators for theoretical study is an infinite linear arrangement. Experimentally the arrangement is necessarily finite [16,17], posing the concern of end effects.

Here we propose to investigate a circular array of toroidal bubble resonators [Fig. 1(a)]. It is a configuration we achieved experimentally due to our expertise with stabilized bubbles in cages. The circular arrangement removes end effects and facilitates analytical predictions. This is an original first step for a periodically ordered bubble-based metamaterial, the first study to the best of our knowledge focusing on matrix-like arrangements [18–20] or disordered arrangements [11].

The goal of the article is to understand the response of an array of toroidal bubbles in this circular configuration. We will also investigate the acoustic field inside the toroidal region of the system looping through the bubbles, whose geometry resembles the toroidal chamber surrounded by magnetics coils whose acronym is "tokamak," used in research on nuclear fusion.

II. METHODS

A. Fabrication

The bubbles are trapped in toroidal cages, designed and fabricated as in [4] using a 3D DLP printer (Anycubic, model Photon zero, z layer thickness = 0.1 mm, with a gray Monocure 3D Rapid Resin). To ensure hydrophobicity, the tori were coated with a water-repellent spray (Mirror Coat Zero, Glaco). This coating effectively fills all the micropores of the photopolymerized resin, creating a hydrophobic, smooth, even surface. The cages consist of an hexagonal mesh of bars, with openings small enough to prevent the entry of water. Note that the cages are fabricated together on a large plate. An example of a fabrication of 12 toroidal bubbles is shown in Fig. 1(b), and all fabricated arrays are photographed in Fig. 2.

———————
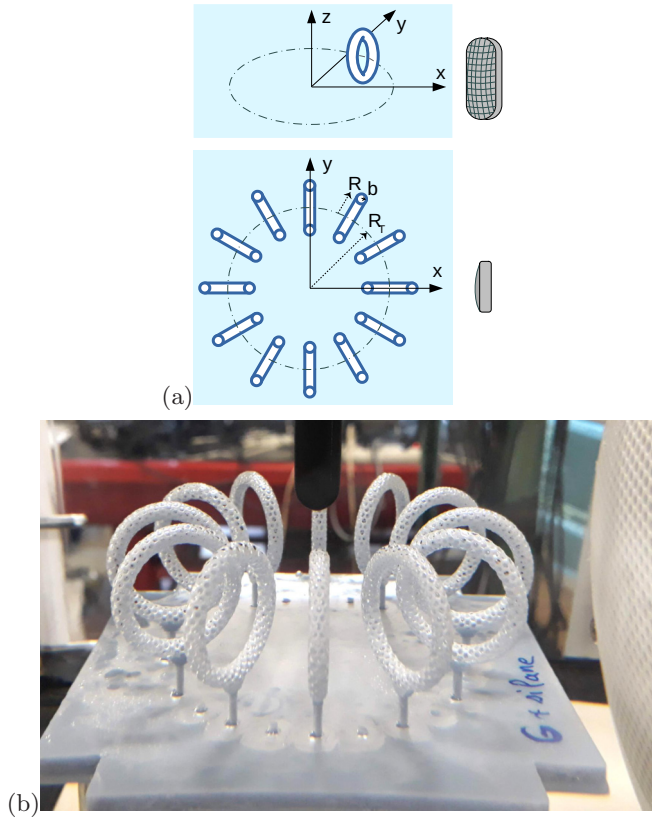[*]philippe.marmottant@univ-grenoble-alpes.fr

FIG. 1. (a) Schematic layout of a circular array of $N = 12$ toroidal bubbles and a loudspeaker on the right. (b) Experimental system of toroidal cages underwater. A hydrophone is placed above the center. The loudspeaker is visible on the right. All tori have a grand radius $R = 11.35$ mm and an aspect ratio $R/b = 7.4$, placed along a circle or radius $R_T = 32.5$ mm.

The crucial step is the immersion of the structure underwater, during which the capillary Laplace pressure across the interfaces acting at the bottom of the structure should counteract the hydrostatic pressure. In practice we found that the vertical immersion of toroidal cages (i.e., with the axis of revolution horizontal), which turned out to be necessary to correctly fill the cages with air, yielded a different interface configuration compared to the horizontal immersion of cages (i.e., when their axis of revolution is vertical) which we used in [4]. Here we found the acoustic resonance frequency of the single torus to be around 1150 Hz when immersed vertically, as compared to about 850 Hz when immersed horizontally (see Appendix A).

FIG. 2. Different fabrications of toroidal cages with different number of tori from $N = 3$ to $N = 24$, placed along a circle of radius $R_T = 32.5$ mm.
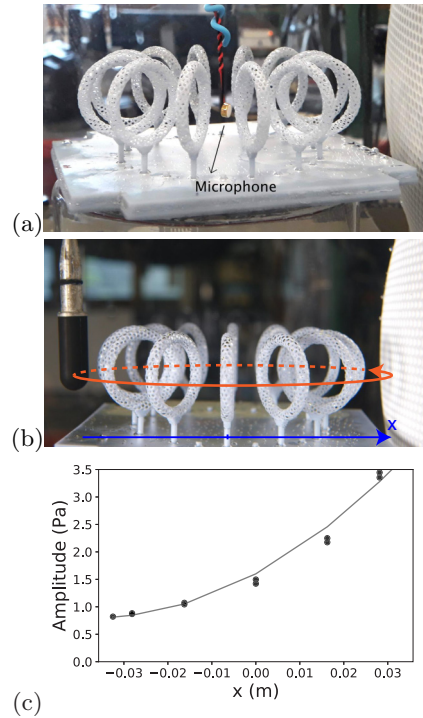

FIG. 3. Spatial measurements. (a) The microphone is displaced between the centers of two consecutive tori. The position closest to the loudspeaker is labeled 0. (b) Hydrophone on the exterior circle near each torus. (c) Distribution of the background sound amplitude measured at each position as in (a) but without the tori (averaged over the spectrum, between 400 and 1800 Hz), showing an increase along the x axis directed to the speaker. The curve is a fit by a quadratic function $P(x) = 1.6[1 + 0.9x/R_T + 0.45(x/R_T)^2]$ in Pa.

B. Acoustic measurements

The experiments are performed in a water tank whose size is 30 cm $\times$ 30 cm $\times$ 25 cm. A frequency sweep is emitted by an underwater speaker placed nearby, and the acoustic pressure is measured with a hydrophone and provides the local acoustic pressure $P(t)$. Because of the steric hindrance due to the size of the microphone, we tested two configurations:

(1) In the middle of two consecutive tori with a small waterproof electret condenser microphone (4 mm in diameter, 2.9 mm in thickness, connected to a preamplifier built from ADA1063, Gotronic) placed as in Fig. 3(a).

(2) Near the outside of each torus with a hydrophone (9 mm in diameter, model no. 8103, Brüel & Kjær) at around 2 mm from each torus as in Fig. 3(b).

The incident pressure is not homogeneous: as seen in Fig. 3(c), it increases near the loudspeaker.

III. ANALYTICAL MODEL

Before presenting the experimental results, we introduce an analytical model which will prove useful in understanding the complex response of our system under an inhomogeneous excitation.

A. Resonance frequency of the assembly of tori

We consider a tokamak with N identical tori on a large circle of radius R_T, numbered from 0 to $N - 1$; see Fig. 1(a). The centers of the tori are evenly spaced on the large circle; hence, we may locate each torus at an angular position $\theta_n = 2\pi n/N$, θ_n being counted from the positive direction of the x axis. With this convention, torus $n = 0$ is the closest to the loudspeaker. Each torus of grand radius R vibrates with a small radius which varies around the equilibrium value b as $b_n(t) = b[1 + \epsilon_n(t)]$, with $n \in \{0, \dots, N - 1\}$ the torus label. We shall henceforth assume small amplitudes of vibration, $|\epsilon_n| \ll 1$.

To describe the interaction between two arbitrary tori n and m, we simplify the problem by assuming that the tori are coaxial (thus neglecting the angle between their orientations). The distance between their centers is $d_{nm} = 2R_T \sin(\theta_{nm}/2)$, with θ_{nm} their angular distance along the large circle. This configuration resembles that of N coupled spherical oscillators, but with a coupling factor specific to the toroidal bubbles, depending only on the distance. Our motivation for this approximation is the following: at large distance the field emitted by a single torus is spherical and does not depend on the angle, while at small distances the tori become closer to the coaxial configuration.

Adapting our previous work on coaxial tori [4] the oscillation of the torus labeled n obeys the equation

$$\rho b \ddot{b}_n \ln \frac{8R}{b} + \mu' \dot{b}_n + 2\gamma p_0 \frac{b_n - b}{b}$$
$$= -\rho b \sum_{m \neq n} \ddot{b}_m \left(t - \frac{d_{nm}}{c}\right) f_t \left(\frac{R}{d_{nm}}\right) - P_n(t), \quad (1)$$

with $f_t(\xi) = \frac{2\xi}{\sqrt{4\xi^2 + 1}} K(\frac{4\xi^2}{4\xi^2 + 1})$ an interaction factor involving K the complete elliptic integral of the first kind, according to [4]. The driving pressure of each torus is $P_n(t)$. Note that an array of spherical pulsators of radius $a_n(t)$ vibrating around an equilibrium value a obeys slightly different equation: $\rho a \ddot{a}_n + 3\gamma p_0 \frac{a_n - a}{a} = -\rho a \sum_{m=0, m \neq n}^{N-1} \ddot{a}_m \frac{R}{d_{nm}} - P_n(t)$ [21]. We include in (1) a phenomenological damping term with a damping coefficient μ', and we include the propagation time of the pressure wave emitted by torus m. The other symbols appearing in (1) are the density of water $\rho = 10^3$ kg/m^3, the adiabatic exponent $\gamma = 1.4$, the ambient pressure $p_0 = 10^5$ Pa, and the speed of sound in water $c = 1.5 \times 10^3$ m/s.

Under a driving pressure field of angular frequency ω, we have $P_n(t) = P_n e^{-i\omega t}$. We neglect the time delays d_{nm}/c. Since Eq. (1) is a linear equation, we can write $\epsilon_n(t) = \xi_n e^{-i\omega t}$, and we get

$$\left(-\omega^2 - i\mu\omega + \omega_0^2\right)\xi_n - \frac{\omega^2}{\ln(8R/b)} \sum_{m \neq n} f_t \left(\frac{R}{d_{nm}}\right)\xi_m$$
$$= -\frac{P_n}{\rho b^2 \ln(8R/b)}, \quad (2)$$

valid for all $n \in \{0, \dots, N - 1\}$. In this equation, ω_0 is the eigenfrequency of an isolated torus, given by $\omega_0^2 = 2\gamma p_0/[\rho b^2 \ln(8R/b)]$, and μ a damping coefficient, related to an attenuation parameter δ by $\mu = \delta\omega_0$. Equation

(2) constitutes a linear system of the form $M\Xi = \Pi$, with $\Xi = (\xi_0, \dots, \xi_{N-1})^T$ the vector of the vibration amplitudes, where ^{T} designates the transpose, $\Pi = -(P_0, \dots, P_{N-1})^T/[\rho b^2 \ln(8R/b)]$ the vector of driving pressures, and M is a matrix such that $M_{nn} = -\omega^2 - i\mu\omega + \omega_0^2$, and if $n \neq m$, $M_{nm} = -\omega^2 f_t(R/d_{nm})/\ln(8R/b)$. Hence, the vibration amplitudes are given by $\Xi = M^{-1}\Pi$ or

$$\xi_n = -\sum_{m=0}^{N-1} (M^{-1})_{nm} \frac{P_m}{\rho b^2 \ln(8R/b)}. \quad (3)$$

To compute the coefficient $(M^{-1})_{nm}$, we note that the matrix M belongs to the class of circulant matrices, which are the matrices such that there exist N complex numbers $c_0, \dots, c_{N-1}$ such that for all $n, m \in \{0, \dots, N - 1\}$, $M_{nm} = c_{n-m}$ if $n \geqslant m$, and $M_{nm} = c_{N-(m-n)}$ if $m > n$. Hence, as all circulant matrices, M possesses the following N eigenvectors: for $p \in \{0, \dots, N - 1\}$, $v_p = (1, e^{2i\pi p/N}, e^{4i\pi p/N}, \dots, e^{2i\pi(N-1)/N})^T/\sqrt{N}$, associated with the N eigenvalues:

$$\lambda_p = \sum_{m=0}^{N-1} M_{0m} e^{2i\pi pm/N}. \quad (4)$$

Moreover, M can be diagonalized as $M = U^*\Lambda U$, where $U_{nm} = e^{-2i\pi nm/N}$, U^* is the complex conjugate of U, and Λ is the diagonal matrix such that $\Lambda_{nn} = \lambda_n$. Hence, $M^{-1} = U^*\Lambda^{-1}U$, from which it is easy to compute $(M^{-1})_{nm} = \sum_{p=0}^{N-1} e^{2i\pi p(n-m)/N}/(N\lambda_p)$. Inserting this expression in (3), we finally get the prediction of the vibration amplitudes:

$$\xi_n = \sum_{p=0}^{N-1} \frac{1}{\lambda_p} \sum_{m=0}^{N-1} \frac{1}{N} e^{2i\pi p(n-m)/N} \Pi_m. \quad (5)$$

This seemingly complicated double sum is actually easy to interpret. The first sum is the superposition of the resonances of each mode, weighted by the spatial projection of the forcing represented by the second sum. Another interpretation is that the discrete Fourier transform of Eq. (2) gives $\tilde{\xi}_p = \tilde{\Pi}_p/\lambda_p$, where $\tilde{\xi}_p = \sum_{m=0}^{N-1} e^{-2i\pi pm/N} \xi_m$ is the transform of ξ_n and $\tilde{\Pi}_p$ the transform of Π_n. Equation (5) follows from the inverse Fourier transform $\xi_n = \frac{1}{N} \sum_{p=0}^{N-1} e^{2i\pi pn/N} \tilde{\xi}_p$.

The resonance of each mode can be deduced from the expression of λ_p given by Eq. (4): $\lambda_p = -\omega^2 - i\mu\omega + \omega_0^2 - \omega^2 \sum_{m=1}^{N-1} e^{2i\pi pm/N} \frac{f_t(R/d_{0m})}{\ln(8R/b)}$, and we have

$$\lambda_p = \left(-\omega^2 - i\mu_p\omega + \Omega_p^2\right)\frac{\omega_0^2}{\Omega_p^2},$$

with the natural frequency of mode p:

$$\Omega_p^2 = \frac{\omega_0^2}{1 + \sum_{m=1}^{N-1} e^{2i\pi pm/N} \frac{f_t(R/d_{0m})}{\ln(8R/b)}}, \quad (6)$$

which is real since the terms in the sum are complex conjugate when switching m to $N - m$. This is the central result of this analytical part.

The vibration associated with this mode has a spatial dependance $\xi_n^{\text{mode } p} = \frac{1}{N} e^{2i\pi pn/N} \tilde{\Pi}_p/\lambda_p$, meaning an oscillation in time with $e^{2i\pi pn/N - \omega t}$, which is a traveling wave rotating
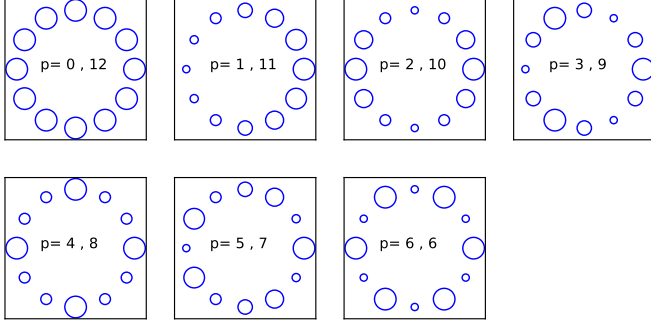
FIG. 4. Illustration of the stationary modes of circular assembly of $N = 12$ bubbles. The circle size represents the amplitude of the small radius oscillation $b_n(t) = b[1 + \epsilon_n(t)]$ at a given time t. A stationary mode is obtained by an equal mixture of propagating eigenmodes p and $N - p$.

around the circle. In practice the frequency Ω_p is degenerated in two modes p and $N - p$, the second rotating in opposite direction $e^{-2i\pi pn/N - \omega t}$. If the forcing is symmetric, we observe a stationary wave which is the superposition of these modes with the same amplitude. This provides a vibration writing $\xi_n \sim \cos(2\pi pn/N)$. We plot in Fig. 4 those stationary modes.

B. Excitation of the modes by a nonuniform excitation pressure

We now study the spatial projection of the forcing, quantified using the Fourier transform $\tilde{\Pi}_p$ of the pressure distribution, for three cases: a spatially uniform forcing, a forcing varying linearly with x, and a forcing with a quadratic dependence on x.

In the case of a uniform forcing, $\Pi_m = \Pi$ independent of m, we have simply

$$\tilde{\Pi}_p = \Pi \sum_{m=0}^{N-1} e^{-2i\pi pm} = N\Pi\delta_{p0}$$

from the known expressions of geometric sums. Hence, only the fundamental mode is forced and (5) reduces simply to

$$\xi_n = \frac{\Pi}{\lambda_0}$$

for every n. Therefore, the fact that experiments show more than one mode is crucially related to the spatial nonuniformity of the pressure field.

Let us now consider the case of a forcing of the form of polynomial of order 2 in x:

$$\Pi = \Pi_a\left[1 + \alpha\frac{x - x_m}{R_T} + \beta\left(\frac{x - x_m}{R_T}\right)^2\right],$$

with Π_a the amplitude felt at the center $x = x_m$ of the large circle. Then each torus perceives the following amplitude:

$$\Pi_m = \Pi_a(1 + \alpha\cos\theta_m + \beta\cos^2\theta_m)$$

$$= \Pi_a\left[1 + \frac{1}{2}\alpha\left(e^{2i\pi\frac{m}{N}} + e^{-2i\pi\frac{m}{N}}\right)\right.$$

$$\left. + \frac{1}{4}\beta\left(e^{2i\pi\frac{m}{N}} + e^{-2i\pi\frac{m}{N}}\right)^2\right],$$
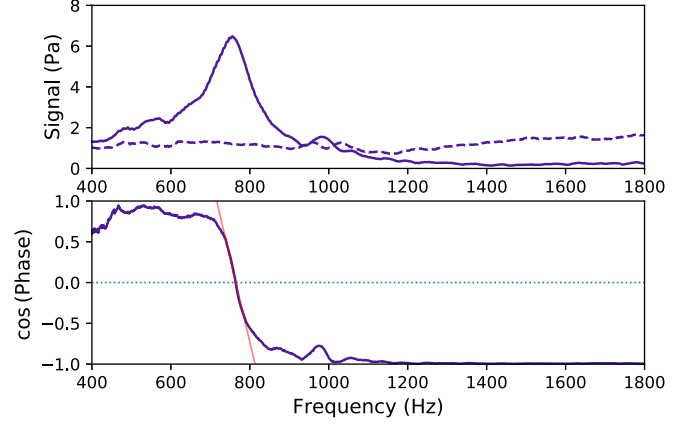

FIG. 5. Fundamental resonance of a tokamak of $N = 24$ tori, placing the microphone at the center as in Fig. 2(a). Top: Amplitude of the signal as a function of frequency. The continuous curve is the measurement with the tori, while the dashed curve is that without the tori (background signal). Bottom: Cosine of the phase of the signal with respect to incoming signal showing a sharp change at resonance. The resonance at occurs at $f_0^{\mathrm{exp}} = 764$ Hz with a quality factor of $Q = 7.9$ measured using the slope of the phase curve at resonance.

whence, using Eq. (5),

$$\xi_n = \Pi_a\left[\left(1 + \frac{1}{2}\beta\right)\frac{1}{\lambda_0} + \frac{\alpha}{\lambda_1}\cos\frac{2\pi n}{N} + \frac{\beta}{2\lambda_2}\cos\frac{4\pi n}{N}\right].$$

A linear forcing along x ($\alpha \neq 0$, $\beta = 0$) forces both the fundamental mode and the mode $p = 1$, but no higher mode. A quadratic forcing ($\beta \neq 0$) will trigger the mode $p = 2$. Similarly it can be shown that spatial forcing with a polynomial of order p in x will trigger up to mode p.

The pressure received at a given observation point is the sum of the incident pressure and of the scattered pressure emitted by the tori. The latter is computed using [4]: $P_{\mathrm{scat}} = \rho \sum_{n=0}^{N-1} \frac{Rb\ddot{b}_n(t-d_n/c)}{\sqrt{(r_n+R)^2+z_n^2}} K\left(\frac{4r_nR}{(r_n+R)^2+z_n^2}\right)$ with d_n the distance between the observation point and the center of torus n, and where r_n and z_n are the coordinates of the observation point (in the local cylindrical coordinates aligned with the axis of each torus).

IV. EXPERIMENTAL RESULTS

A. Fundamental mode of the tokamak assembly

We recorded pressure signals $P(t)$ and a reference signal without bubbles $P^0(t)$ after the removal of the assembly. We plot in Fig. 5(a) an example of the Fourier transforms $\hat{P}$ and $\hat{P}^0$ of the pressure signals. The background emission $\hat{P}^0$ is relatively homogeneous. We also compute the relative contribution of the bubbles to the signal using $A = (\hat{P} - \hat{P}^0)/\hat{P}^0$, and in particular its phase ϕ. To avoid unwrapping the phase we prefer to plot $\cos(\phi)$.

The acoustic response is first recorded by placing the microphone above the center of the assembly, at an equal distance to all the toroidal bubbles, as in Fig. 2. The spectrum of the measured signal shows a clear resonance when looking at the amplitude of pressure (see Fig. 5), reminiscent of a harmonic oscillator. We assume that the response A is given
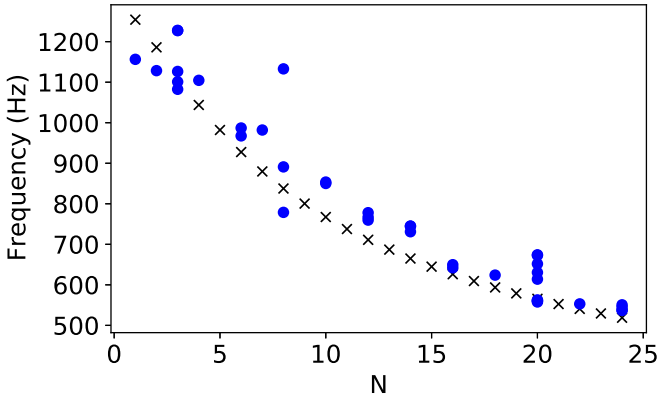
FIG. 6. Resonance frequency for different number of tori (circles), microphone in the center. Analytical model (crosses) from Sec. III.

by a driven harmonic oscillator equation writing $(-\omega^2 - i\omega\omega_0/Q + \omega_0^2)A = F$ in harmonic notation, with ω_0 the resonance pulsation, Q the quality factor, and F a forcing term. The response A of the harmonic oscillator has a phase ϕ with respect to driving, whose cosine writes $\cos(\phi) = (-\omega^2 + \omega_0^2)/\sqrt{(-\omega^2 + \omega_0^2)^2 + \omega^2\omega_0^2/Q^2}$. The cosine vanishes at the the frequency such that $\omega = \omega_0$ and the slope of the cosine versus frequency is $d\cos(\phi)/d\omega = -2Q/\omega_0$ at resonance. We thus define the resonance frequency f_0^{exp} as the frequency at which $\cos(\phi)$ crosses the value 0, and the quality factor is obtained from the slope of the phase curve at resonance, using $Q = -d\cos(\phi)/df \times f_0/2$.

The fundamental resonance frequency decays sharply with the number of tori N in the assembly (see Fig. 6), reflecting the increased proximity of tori at higher N. It is well fitted by the model, using the fundamental mode $p = 0$ in Eq. (6), adjusting the inner radius b to 1 mm (resulting in 1250 Hz for one toroidal bubble, slightly higher than the measured value).

B. Detection of all modes

Above the frequency ω_0, the vibrations of all the tori are not in phase, which is the signature of higher-order modes. In order to detect such modes, where the phase of the vibrations can be spatially inhomogeneous, we performed measurements by placing the microphone as close as possible to each individual torus.

The first method with a small condenser microphone between tori gives a stronger signal but equally measures the emissions from the two neighboring tori. In order to discriminate emission from individual tori, especially for a low N number, we preferred the second method with a larger hydrophone on the outer circle [see Fig. 3(b)].

Measurements for $N = 12$ clearly feature a common fundamental resonance peak [Fig. 7(a)]. Notice that the acoustic field is enhanced up to 20 times in locations that are away from the loudspeaker (position 6). Each torus features higher resonances modes whose frequency depends on the torus number. The tori are not in phase with each other above the fundamental resonance [Fig. 7(b)]. We also plot in Fig. 7(c) the dispersion of the phases, using the standard deviation among

the N tori [see Fig. 7(c)]; we shall show now that this measure is useful to detect the eigenfrequencies of higher-order modes.

C. Frequency of the modes

The model predictions, plotted in the right column of Fig. 7 also feature several peaks at the resonance of the modes. We observe the following feature on the phase of the modes: at the resonance of modes 1 and 2 the phases tend to approach or cross the value $\pi/2$ [$\cos(\phi) = 0$]; see Fig. 7(e) showing the predicted phase. We thus identify relative minima in the standard deviation of the phases as the frequency f_1^{exp} and f_2^{exp} of modes $p = 1$ and $p = 2$; this turned out to be the most reliable way to measure experimentally these frequencies.

We plot in Fig. 8 the frequency of the modes detected with this method for different numbers of tori. The agreement between the model and the data is also good for these two modes, although slightly less good than for the fundamental mode. The model reproduces the fact that these frequencies decrease at increasing number of tori, but slightly overestimate the eigenfrequencies of modes 1 and 2. The modes 2 detected are excited only with a nonuniform quadratic excitation along x. We could check this point by performing another experiment (data not shown) with a tokamak facing the loudspeaker, with a much more homogeneous pressure field, and no quadratic excitation along x.

D. Spatial distribution of the response

The spatial distribution of the amplitudes along the tokamak is shown in Fig. 9 (left column). The amplitude of mode 0 is remarkably uniform all around the tokamak, in spite of the nonhomogeneous excitation shown in Fig. 3(c). This is confirmed with many experiments, monitoring the response for different tokamak.

The spatial distribution of the phases (as a function of the angle) is plotted in Fig. 9 (right column). All tori are in phase at mode 0. For mode 1, all phases near the loudspeaker, around angle 0°, have a value of $\cos(\phi) = -1$, except in a wide region opposite to the loudspeaker, around angle 180°, were the phase is nearly opposite, which is consistent with a stationary wave with two nodes. For mode 2, the angular pattern is not as clear, but we distinguish two peaks, suggesting two regions or diverging phase around 90° and 270°, while the regions around 0° and 180° have a value of $\cos(\phi) = -1$.

E. Comparison of experiments with the analytical model

The model correctly captures the location of the peaks in pressure (first row of Fig. 7), although not with the same amplitude. The pressure at very high frequency tends to be much less than the reference pressure. This phenomenon is typical of metamaterials, where all subwavelength resonators emit out of phase and thus tend to cancel the incident wave [20].

In the model we have adjusted the resonance frequency of a single torus to $f_0 = 1250$ Hz, by tuning the small radius to the value $b = 1$ mm to fit the assembly of tori immersed vertically, instead of $b = 1.53$ mm as observed for tori immersed horizontally as in [4]. Such a difference in the fitting of the effective radius r originates from the fact that the
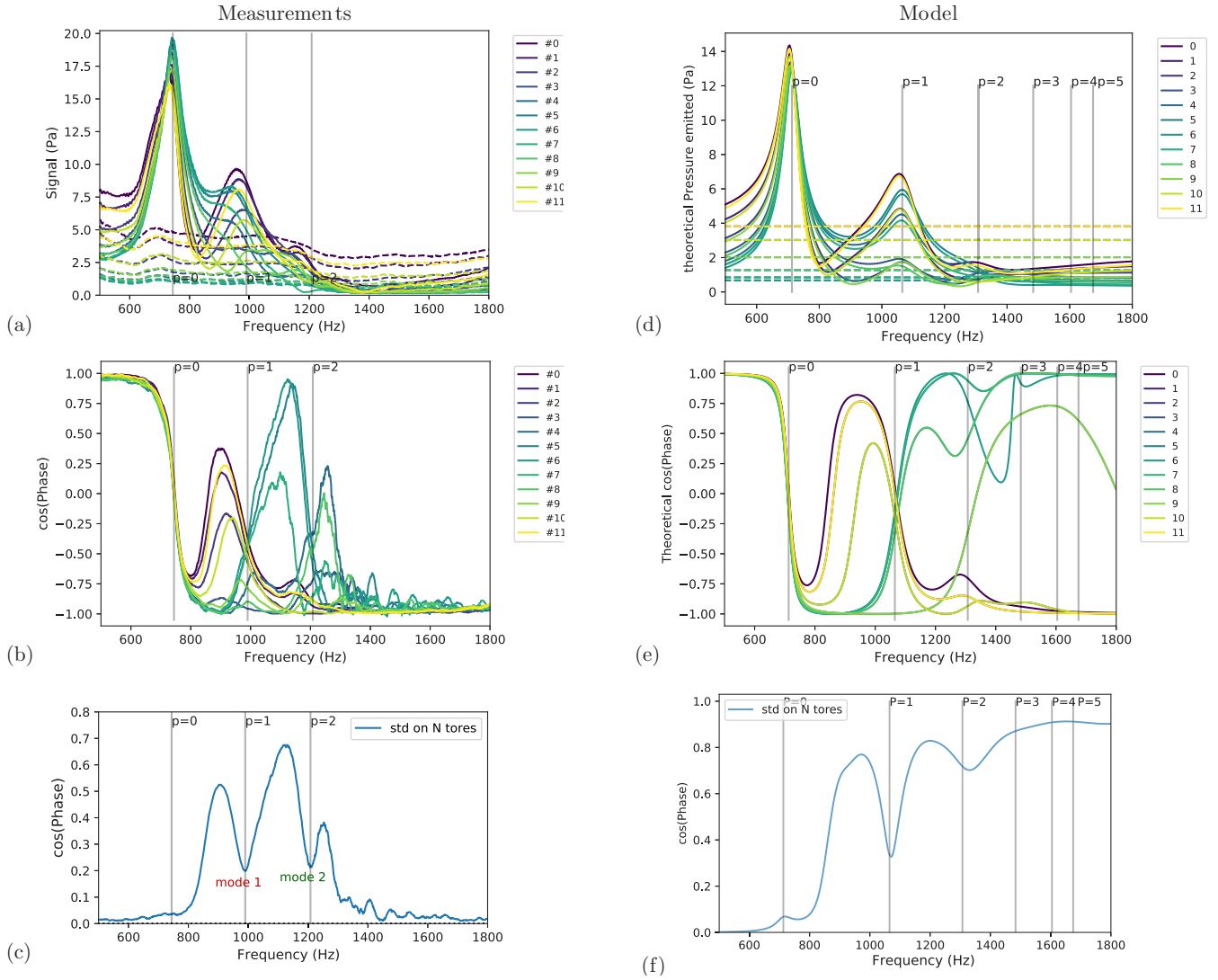
FIG. 7. Measurements (a)–(c) and model (d)–(f) for the pressure near each torus. (a), (d) Spectrum obtained with the tokamak $N = 12$ (lines) and reference measured without (dashes) at different positions between tori (labeled 1 to 12). (b), (e) Cosine of the phase of the signal with respect to the excitation. (c), (f) Standard deviation of the cosine of the phase. Measurements are made with a tiny condenser microphone. Model according to Sec. III, with the following parameters: $R_T = 32.5$ mm, $R = 11.35$ mm, $b = 1$ mm (fitted value to obtain the same resonance frequency as in experiment; design was 1.5 mm), and attenuation $\delta = 1/Q = 1/8$. Nonuniform excitation profile using the experimental fit (Fig. 3). The incident plus scattered pressure is calculated between the centers of the tori n and $n + 1$, at the same location as the experiments [a small offset of $+0.2$ Pa is introduced on curves 6 to 11 in panel (d) to disentangle overlapping curves].

angle of immersion impacts the location of the interface (see Appendix A).

We now have to check that the approximation in our model, tori interacting as if they were coaxial, is justified.

V. FINITE-DIFFERENCE TIME-DOMAIN SIMULATIONS

In this section we use 3D finite-difference time-domain (FDTD) numerical simulations to complement the analytical model introduced in Sec. III. Results from 3D FDTD simulations are first confronted to predictions from the analytical model, and are then further analyzed to exploit information not available from the analytical model.

A. Methods

We followed the same simulation approach introduced in our earlier work [2–4], whereby we investigated the vibrations of air bubbles of various shapes in water. Briefly, air bubbles in water are described in our FDTD simulations through binary maps discretized over a Cartesian mesh with a given spatial resolution. Both water and air are considered ideal lossless fluids. The shapes of the bubbles are limited only by the resolution of the mesh. All the simulations involve toroidal structures with the same dimensions already used for the theoretical predictions (small radius $b = 1$ mm, grand radius $R = 11.35$ mm, and $R_T = 32.5$ mm). The resolution of the mesh (grid step h) was chosen small enough to obtain
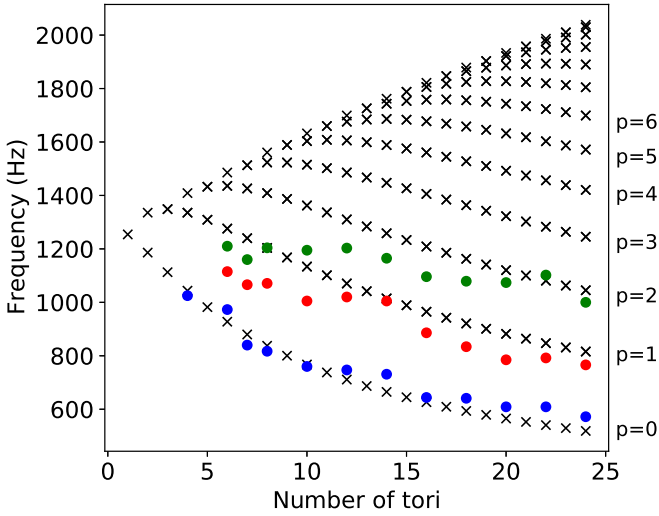
FIG. 8. Detection of the modes 1 and 2 from the minima of the standard deviation (circles). Analytical model: crosses; see Sec. III.

converged results, i.e., results with no significant differences when compared to smaller grid steps, while maintaining practical computation times. In practice, simulations with a step size from $h = 0.5$ mm down to $h = 0.25$ mm led to a relative difference in mode frequencies of less than 0.5%, which was thus considered as an upper bound on the relative accuracy for our FDTD-predicted mode frequencies. In the kHz frequency range relevant here, h was always much smaller than the typical wavelength (about 1 m in water and a few tens of cm in air), and also much smaller than the smallest torus dimension ($b = 1$ mm).

For all simulations, a Gaussian pulse excitation waveform with center frequency f_0 (ranging from 800 to 1800 Hz) and a fixed relative bandwidth (50%) was emitted by a selected set of point sources, specific to each bubble geometry: to preferentially excite a given stationary mode (N, p), N point sources were placed at the centers of the N tori, with amplitudes $A_n(N, p)$ for the nth torus corresponding to the spatial profile of the targeted mode:

$$A_n(N, p) = A_0 \cos\left(2\pi \frac{np}{N}\right). \qquad (7)$$

The center frequency f_0 was chosen based on the desired mode to excite, with typically $f_0 = 800$ Hz used to excited modes with frequencies in the range [600–1200 Hz], and $f_0 = 1800$ Hz used to excited modes with frequencies in the range [1600–2000 Hz].

Perfectly matched layers were set around the simulation domain to simulate the vibration of the structure in free space, consistent with the theoretical model. It was also verified that when a vibration structure is located at the center of a reverberant cavity of linear size typically a few tens of centimeters, representative of the experimental situation, the eigenmodes had the same pattern and resonant frequency than for the free-space situation within the accuracy of the FDTD simulations.

For each simulation, pressure waveforms were recorded at various receiver positions, including receivers placed at the center of each torus. The resonant frequency was derived
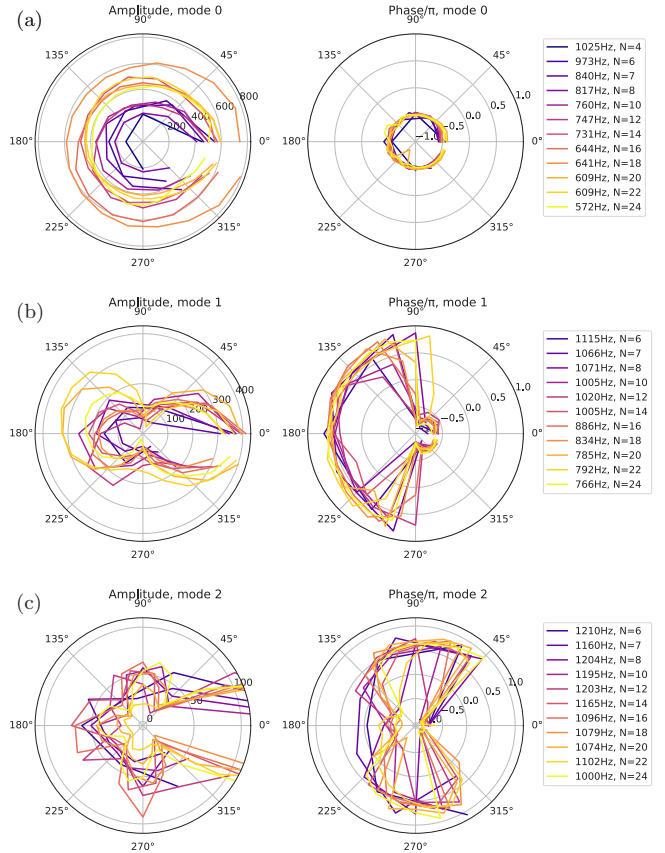

FIG. 9. Angular distribution of the amplitude (mV, with 800 mV in the electrical signal corresponding to a sound pressure of 30 Pa) and phase (divided by π) showing similar patterns among different N for (a) mode 0 at frequency f_0^{exp}, (b) mode 1 at frequency f_1^{exp}, and (c) mode 2 at frequency f_2^{exp}.

from the frequency spectrum of the received signals, after the impulse excitation was time-gated out of the signal. The center frequency of the excitation pulse was adjusted such that only one mode of interest was preferentially excited, in addition to optimizing the phase and amplitude of the set of N sources. In this case, the measured signals were quasimonochromatic, with only one peak in the frequency spectrum.

B. Results

1. Eigenmodes for N = 12

As a first qualitative illustration of FDTD simulations results, Fig. 10 shows the seven stationary eigenmodes ($p = 0, \ldots, 6$) obtained for the structure with $N = 12$ tori. These patterns correspond to the pressure fields associated with the schematic representation provided in Fig. 4.

2. Comparison of frequency predictions from FDTD simulations and the analytical model

FDTD simulations were computed for a range of values N from 1 to 24. The resonance frequency of all the simulated modes is shown in Fig. 11 (circles), together with the values predicted from the analytical model (crosses). The predictions from the FDTD simulations and the analytical model
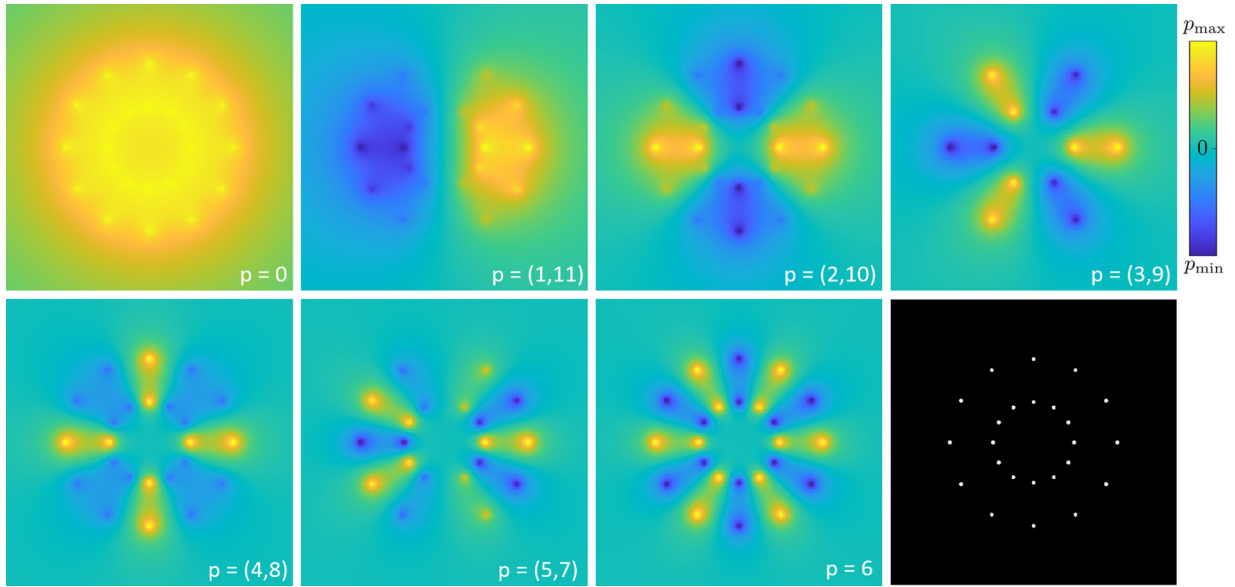
FIG. 10. The seven stationary eigenmodes for $N = 12$ tori, computed with FDTD simulations. Each pattern corresponds to a cross-sectional pressure snapshot taken at a time when the pressure is maximum on torus 1 located on right. The binary image shows a cross section in the same plane of the discretized stucture, with a mesh size of 0.25 mm. White pixels show the position of the air in this cross section, and the liquid is in black.

are in excellent agreement for the smallest modes (less than typically 0.1% relative difference), and a small but significant difference is observed typically for values of $p \gtrsim 4$ and $N \gtrsim 15$. For instance, for $p = 4$ and $N = 24$, the resonance frequency predicted by the analytical model (1421 Hz) is 2.2% lower than that predicted from the FDTD simulations (1453 Hz). As discussed in the Methods section, it was carefully checked that FDTD simulations results were converged in terms of frequency measurements with a relative accuracy better than 0.5%, provided results that we considered as our reference, within the frame of our lossless model in

a infinite medium. It can thus be concluded that the analytic model slightly underestimates the resonance frequency for large values of p and N, although this relative underestimation remains below 3%: the largest relative difference (-2.5%) was observed for $N = 24$ and $p = 5$.

The excellent general agreement illustrated by Fig. 11 indicates that the coaxial approximation that was used to assess the coupling between two different tori is a very good one in most cases. The slight discrepancy observed for large values of p may be interpreted by the fact that for modes with large values of p, the pressure field has stronger gradients from one torus to its immediate neighbors (see, for instance, Fig. 10), and the coupling between neighboring tori may be less important than coaxial tori. It also seems rather intuitive that considering only the distance from torus to torus without taking account their relative orientation should break down for tori closer to each other than their own radius. As illustrated in Fig. 12 for $N = 1$, the field scattered by a single torus is close to monopolar spherical field outside the torus: as a consequence, the relative orientation between tori is expected to play a role only for tori very close to each other, for a distance of the order of their own radius. Interestingly, the analytical model remains relatively accurate even at its limits, probably because the coupling terms are well estimated for most pairs of tori, and biased only for immediate neighbors.

Our excellent agreement between the analytical model and the FDTD simulations also indicates that the difference between the theoretical frequencies and the experimentally measured ones is caused by other phenomena not taken into account in our lossless models with only radiative damping. It is likely that significant dissipative phenomena related to the presence of the 3D-printed frames holding the toric bubbles have a significant influence on the resonance frequency and quality factor of resonances observed experimentally. In our FDTD simulations, we observed that exciting high-order
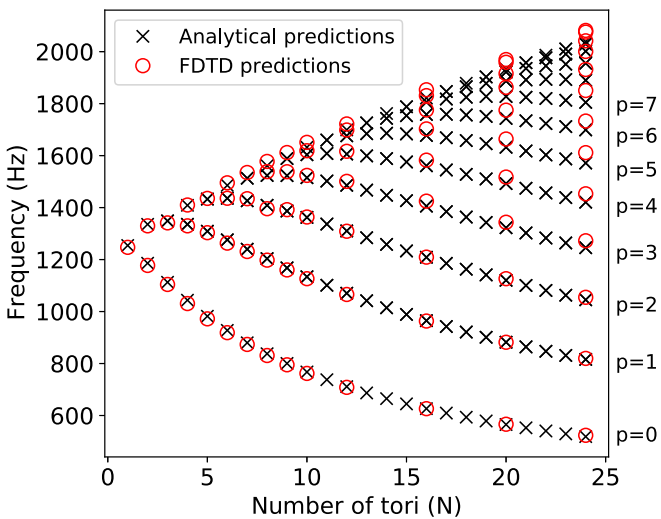

FIG. 11. Resonance frequencies of the eigenmodes predicted from the analytical model (black crosses) and from the FDTD simulations (red circles). For modes $p \geqslant 4$, the analytical model slightly underestimates the resonance frequency, as compared to that predicted from FDTD simulations.
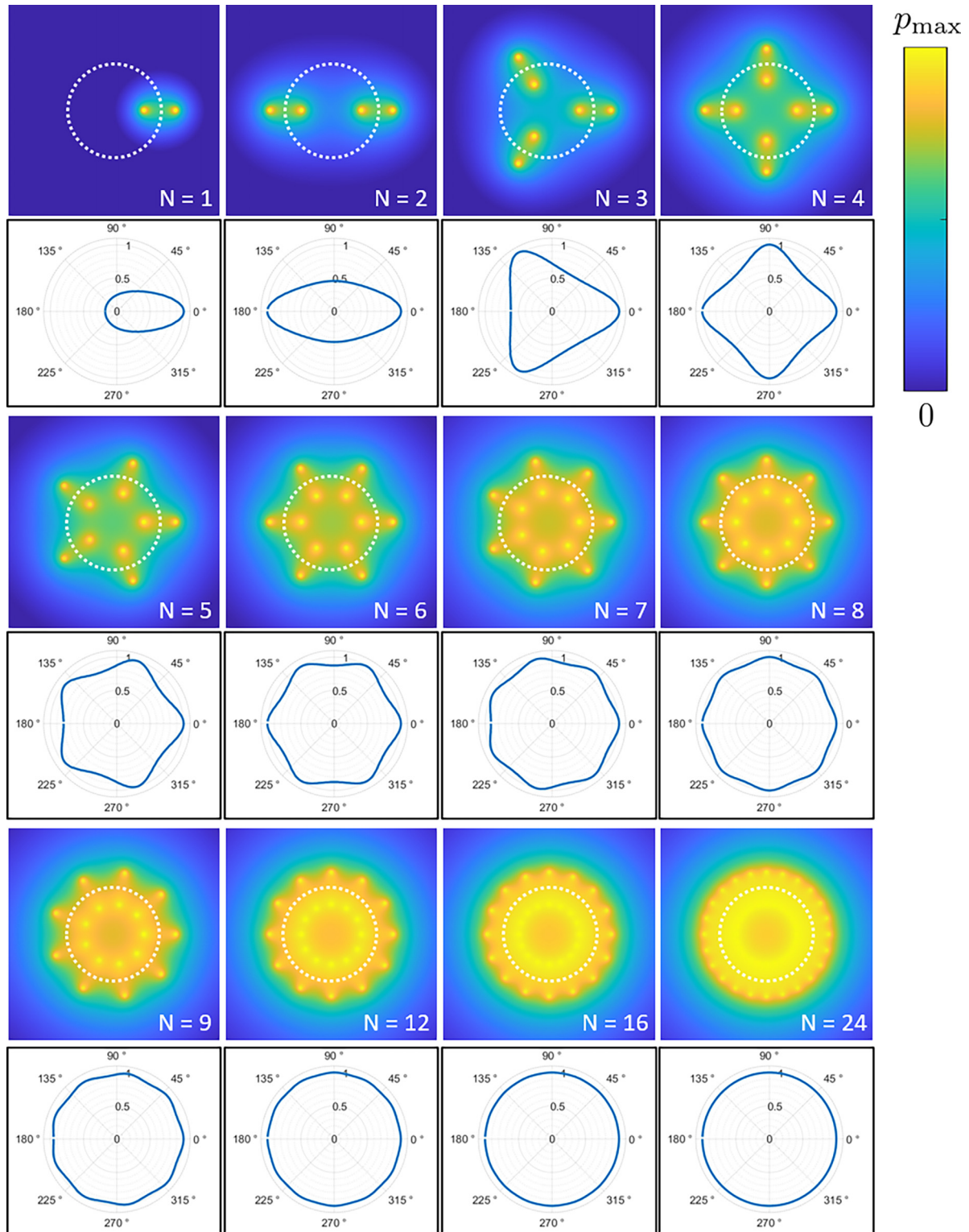
FIG. 12. Fundamental mode ($p = 0$) for different number of tori. For each N, the polar plot represents the normalized pressure amplitude measured in the main plane at receivers distributed along the big radius of the structure, i.e., the central radius of the tokamak (white dashed line).

modes is possible only by setting multiple sources matching the mode patterns. With a single source as used in our experiments, only modes $p = 0$, 1, or 2 may be efficiently excited, explaining why mode orders above 2 have not been observed here, to our best knowledge.

3. FDTD simulations of the fundamental mode ($p = 0$)

As compared to our analytical approach, which models each individual torus as a pointlike resonator, our FDTD simulations provide access to the spatial distribution of the pressure field at a scale down to that of each individual torus. In

particular, it is straightforward by recording snapshots to investigate the pressure distribution inside the tokamak, whereas such a pressure field is difficult to measure experimentally because of the finite size of the hydrophone.

Figure 12 shows the pressure patterns of the fundamental vibration mode ($p = 0$) for N ranging from 1 to 24. Note that because the pressure varies in phase everywhere for the fundamental mode, the colorscale now represents only positive amplitude values, as opposed to that in Fig. 10, which describes in-phase and opposite-phase regions. The polar plots represent the normalized pressure amplitude measured with receivers distributed along the tokamak central line (white dashed line). Figure 12 illustrates that the pressure field inside the tokamak tends to become more and more homogenous when the tori get more and more densely packed for large N. In particular, the polar plots shows that the pressure amplitude assessed along the central radius varies less than 5% starting from $N = 9$.

Looking at the details of the field around the tori in Fig. 12, we can see that there are two cases where the approximation neglecting angles between tori could hold: first, when N is very large (N greater than 9), since the bubbles are nearly coaxial, and then when N is very small (N until 3), since the tori are far from each other, and the field emitted far away is mainly spherical and does not depend on the angle of the emitting torus.

VI. CONCLUSIONS

We explored the resonance of this original circular metamaterial and found a model to account for the frequency of the modes as well as for the spatial patterns. The approximation of coaxial tori was sufficient to provide a very good prediction of the first modes.

Perspectives include the experimental characterization of the acoustic field in the center of the tokamak, where the emitted pressure becomes quasihomogeneous in an extended region of space. Having a homogeneous field could

FIG. 14. Vertical immersion of a torus: top part of the torus (top image) and bottom part (bottom image).

prove useful in the study of objects moving in the center, while experiencing the same amount of sound during their motion.

Auxiliary information regarding the resources used in this work is supplied in the Supplemental Material [22].
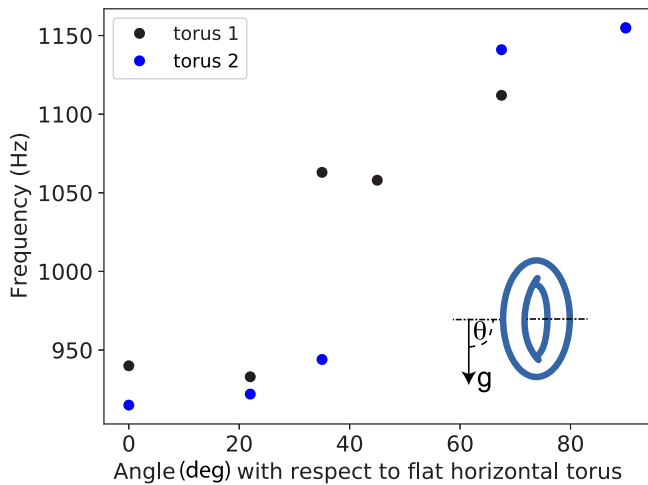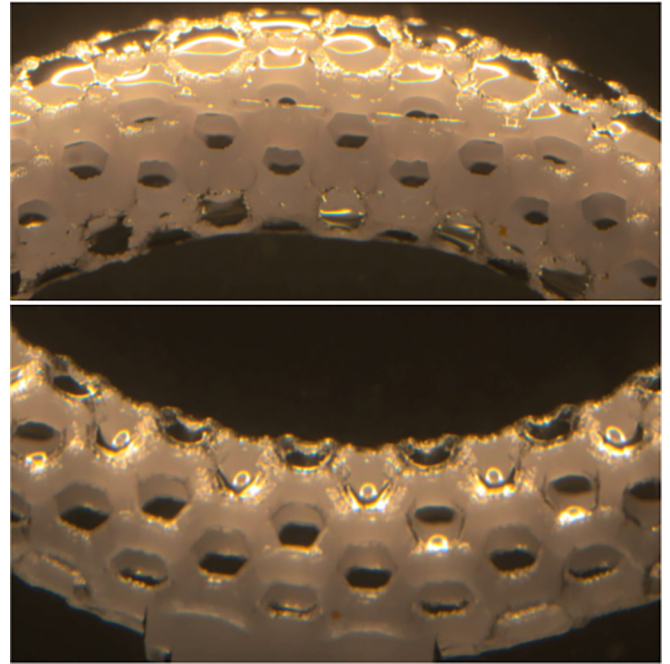
FIG. 13. Fundamental resonance frequency of a single torus when dipping it with different orientation (experiments on two different tori). The angle is the angle of the revolution axis with respect to the gravity vector; see drawing.
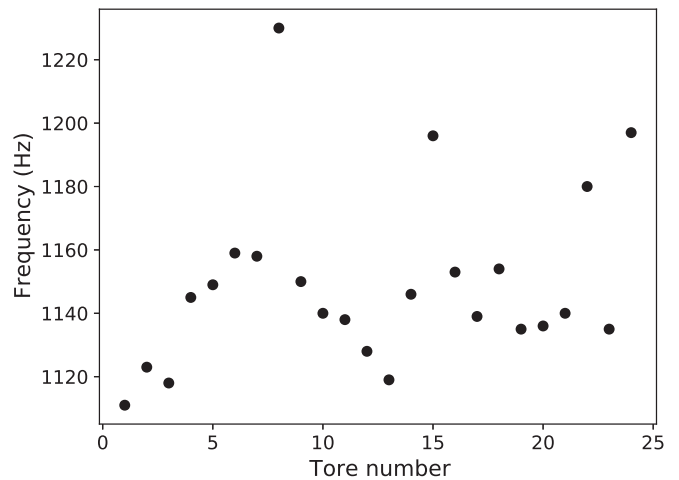

FIG. 15. Resonance frequency of tori in 24 as a function of its number along the circular arrangement, from 1 to 24. The mean is 1150 Hz and standard deviation 27 Hz.

APPENDIX A: RESONANCE OF A SINGLE TORUS, INFLUENCE OF THE DIPPING ANGLE

The tori are immersed in a vertical position, as illustrated in Fig. 2. When dipping individual tori with varying angles, we found that the resonance frequency increases when the torus is closer to vertical (Fig. 13). This explains why the tori used in this study featured a frequency around 1150 Hz, compared to previous measurements when dipping the same tori flat (around 850 Hz [4]). Actually, we observed that when dipped vertically, the tori presented air-water interfaces bulging more inwards in the open windows between the cages, as compared to a horizontal dipping, especially at the bottom part of the torus (Fig. 14). This could explain the dependence of the resonance frequency on the angle of immersion, and also why we need to take smaller values of the small radius to fit our experimental results (see Sec. IV A).

APPENDIX B: VARIABILITY OF THE RESONANCE OF TORI IN A TOKAMAK

In order to assess the uniformity of the tori, we have cut out each torus of the assembly with $N = 24$, and measured it separately. We show in Fig. 15 limited variations of frequencies of $\pm 2\%$.

[1] F. Lemoult, M. Fink, and G. Lerosey, Phys. Rev. Lett. **107**, 064301 (2011).

[2] M. Harazi, M. Rupin, O. Stephan, E. Bossy, and P. Marmottant, Phys. Rev. Lett. **123**, 254501 (2019).

[3] M. Boughzala, O. Stephan, E. Bossy, B. Dollet, and P. Marmottant, Phys. Rev. Lett. **126**, 054502 (2021).

[4] M. Alloul, B. Dollet, O. Stephan, E. Bossy, C. Quilliet, and P. Marmottant, Phys. Rev. Lett. **129**, 134501 (2022).

[5] K. Marinov, A. D. Boardman, V. A. Fedotov, and N. Zheludev, New J. Phys. **9**, 324 (2007).

[6] Y.-W. Huang, W. T. Chen, P. C. Wu, V. Fedotov, V. Savinov, Y. Z. Ho, Y.-F. Chau, N. I. Zheludev, and D. P. Tsai, Opt. Express **20**, 1760 (2012).

[7] T. J. Zimmerling and V. Van, Opt. Lett. **45**, 714 (2020).

[8] S. W. Yoon, L. A. Crum, A. Prosperetti, and N. Q. Lu, J. Acoust. Soc. Am. **89**, 700 (1991).

[9] C. Feuillade, J. Acoust. Soc. Am. **98**, 1178 (1995).

[10] A. A. Doinikov, J. Acoust. Soc. Am. **116**, 821 (2004).

[11] V. Leroy, M. Devaud, T. Hocquet, and J. C. Bacri, Eur. Phys. J. E **17**, 189 (2005).

[12] E. M. B. Payne, S. J. Illesinghe, A. Ooi, and R. Manasseh, J. Acoust. Soc. Am. **118**, 2841 (2005).

[13] Z. Zeravcic, D. Lohse, and W. van Saarloos, J. Fluid Mech. **680**, 114 (2011).

[14] K. S. Spratt, K. M. Lee, P. S. Wilson, and M. F. Hamilton, JASA Express Lett. **2**, 036001 (2022).

[15] M. Strasberg, J. Acoust. Soc. Am. **25**, 536 (1953).

[16] O. Richoux and V. Pagneux, Europhys. Lett. **59**, 34 (2002).

[17] X. Ni, K. Chen, M. Weiner, D. J. Apigo, C. Prodan, A. Alù, E. Prodan, and A. B. Khanikaev, Commun. Phys. **2**, 55 (2019).

[18] V. Leroy, A. Strybulevych, M. G. Scanlon, and J. H. Page, Eur. Phys. J. E **29**, 123 (2009).

[19] A. Bretagne, A. Tourin, and V. Leroy, Appl. Phys. Lett. **99**, 221906 (2011).

[20] V. Leroy, A. Strybulevych, M. Lanoy, F. Lemoult, A. Tourin, and J. H. Page, Phys. Rev. B **91**, 020301(R) (2015).

[21] T. Combriat, P. Rouby-Poizat, A. A. Doinikov, O. Stephan, and P. Marmottant, Soft Matter **16**, 2829 (2020).

[22] See Supplemental Material at http://link.aps.org/supplemental/10.1103/PhysRevE.108.045105 for the resources used in this work.